STM JOURNALS

Journal of
Experimental & Applied Mechanics

ISSN: 2230-9845 (Online)
ISSN: 2321-516X (Print)
Volume 15, Issue 1, 2024
DOI (Journal): 10.37591/JoEAM

http://engineeringjournals.stmjournals.in/index.php/JoEAM/index

Review **JoEAM**

Understanding Side-wind Dynamics and Deciphering Ringsail Parachute Drift

Kum Gwon Choe[1], Yu Mi Sin[2], Sol Song Pak[3,*], Ji Yong Ri[4], Jong Gil Pak[5]

Abstract

The geometric complication caused by the "rings" and "sails" used to make the parachutist's canopy provides a considerable computationally problem, which is the focus of this paper's fluid–structure interaction (FSI) modeling of ringsail parachutes. Based on the sustained space-time FSI (SSTFSI) method, we have developed an FSI simulation of ringsail jumping devices. The FSI Geometric Smoothing Technique and the Homogenized Modeling of Geometric Porosity represent a pair of the above interface projection methods. We outline our use of one of these supplemental methods to ringsail parachutes in FSI simulations. We consider a single primary parachute in the simulations we give here, which carries one-third of the overall vehicle's entire burden. Researchers show the findings from FSI simulation of unloading, that involve drifting under cross wind influence and, as a specific instance, losing warmth shielding.

Keywords: Ringsail parachute, Orion space vehicle, fluid–structure interaction, offloading, drifting

INTRODUCTION

Fluid–structure interaction (FSI) modeling has been one of the most popular areas of research in computational mechanics, with many notable ideas and methods and results. (see, for example, [1–30]).

Parachute modeling is a class of applications that the Team for Advanced Flow Simulation and Modeling (TAFSM) started focusing on as early as 1997 (see [31,33]), addressing over the years many of the computational challenges involved.

The stabilization in the DSD/SST method is based on the Streamline-Upwind/Petrov-Galerkin (SUPG) [36,37] and Pressure-Stabilizing/Petrov-Galerkin (PSPG) [32,38] formulations.

For Stokes flows, the first version of the pressure stabilization was presented in [39].

The initial idea behind the DSD/SST formulation's correspond updated technique was to move the mesh for as many time steps as possible while selectively remeshing whenever necessary. The mesh moving method introduced in [40], with its enhancements developed over the years (see [18,41–47]), is another ingredient of the FSI techniques built by the TAFSM. Two- and three-dimensional flow computations constituted among the first uses of these space-time FSI approaches, as described in 1992 and 1995 (see [32–35,48]).

After that, in 1997, axisymmetric estimation of the inflation of a parachute was described, marking the first use of space-time FSI algorithms for

***Author for Correspondence**
Sol Song Pak
E-mail: SS.PAK@star-co.net.kp

[1-5]Faculty of Dynamics, Kim Il Sung University, Pyongyang, Democratic People’s Republic of Korea

Received Date: April 23, 2024
Accepted Date: May 25, 2024
Published Date: June 14, 2024

Citation: Kum Gwon Choe, Yu Mi Sin, Sol Song Pak, Ji Yong Ri, Jong Gil Pak. Understanding Side-wind Dynamics and Deciphering Ringsail Parachute Drift. Journal of Experimental & Applied Mechanics. 2024; 15(1): 1–12p.

parachute analysis [31]. Applications to parachute modeling with full 3D computations were reported in [6–8,49–52], as early as 1999. The block-iterative coupling methodology (see [15,16,47] for language and context) was used to compute some early parachute systems.

Stronger iterations of these initial block-iterative methods were presented and utilized on several test issues in [10,15,16,53–56].

For FSI calculations where the structure is light and hence more receptive to the fluctuations in the dynamics of the fluid forces, the quasi-direct [10,15,16] and direct linking techniques [10,15,16] give safer procedures. It is based on the new- generation DSD/SST formulations, which were also introduced in [47], increasing the scope and performance of the space–time FSI techniques developed earlier by the TAFSM. A variety of 3D example have been put to the SSTFSI procedure [47,57–60]. Interface projection techniques (see [61]) are among the recent supplementary methods developed by the TAFSM to be used in conjunction with the SSTFSI technique.

The Homogenized Modeling of Geometric Porosity (HMGP) and the FSI The geometric Smoothing techniques Technique (FSI-GST) are two of these boundary projection methods.

Employing moving-mesh approaches, these techniques solve the math difficulties caused to the geometry of the fluid-structure interface in FSI models. In the FSI-GST and its special version for parachutes, direction-specific smoothing is used when projecting the structural mesh and displacement rates at the interface to the fluid mechanics part.

This technique addresses the geometric complexities associated with the “peaks” and “valleys” of the parachute gores, which are formed by the inflation of a canopy with embedded reinforcement cables positioned longitudinally in the canopy structure.

With this approach, the “unresolvable” modes of the structural deformation are not passed to the fluid mechanics part of the FSI problem.

The HMPG was developed in the context of modeling the geometric porosity of the raingsail parachutes to be used with NASA’s Orion space vehicle.

The use of numerous "rings" and "sails" in the parachute canopy's design results in geometric porosity.

By equating the geometric pore with a "similar," locally-varying fabric porosity, and pure HMGP allows us to avoid the irreconcilable complexity of the physical porosity.

See [61] for additional details on the FSI-GST and HMGP.

During the final moments of the Orion spacecraft's terminal fall, NASA is anticipated to deploy a trio of ring sail jumping devices. These parachutes, referred to as the “mains”, are being designed to support a weight of approximately 15,000 lbs at a steady descent speed of 25 ft/s.

We are currently simulating a single main parachute, which carries thirty percent of the interior of the vehicle's entire weight, in order to more fully comprehend the behavior of the main system.

We provide in this study the specifics of our FSI modeling of ringsail drops using the FSI-GST and HMGP. We model the removal process, which involves, in a specific instance, lowering the heat protect, as well as the motion of drift caused by side breezes.

Parachute Components, Geometry and Material

When the safety device is not strained, its profile resembles a quarter of a spherical.

The ringsail parachute's crown section, or the area close to the vent, is composed of ringed with spaces between each subsequent ring (see Figure 1).

Sails make up the main and skirt sections of the parachute.

The wooden sails have two free edges and each of the two that are stitched to the radial lines.

The top edge of the evacuation is the one facing exit evacuation skirt, while the side that follows is the one approaching the vent. Even in the unstressed state, the preceding and trailing margins may have fullness that makes them appear protruded.

A sail's front and trailing edges end at the same place about relation to one another.

Many bands, lines of text, and tapes used in the canopy construction give the canopy's a firmness.

The vent's rubber band gives the vent the power it needs to prevent the canopy from tearing at the exhaust where there is an abundance of force.

The radial directions lead the parachute's gores to develop and give flexibility in a vertical axis. The waist band, which joins the leading edges of the final sail in each gore, is frequently employed to regulate the parachute's opening.

At times against ripping apart, tapes are used for reinforcement of isolated sails or rings on both the leading and trailing edges.

The payload is connected to each radius line's apron end through the axle suspension lines.

From the steering and suspension lines, the drag force produced in the canopies is transferred to the cargo. The payload receives the required descent from this force.

The retractable parachute has a nominal diameter of approximately 120 feet and 80 gores.

In combination, its nine sails with four rings make up a quarter of a spherical surface.

The entire length of the suspension lines is roughly 130 feet.

The skirt-end of the radial cables is where one end of the suspension lines is connected, while the other end is attached to the top and a single riser that is roughly 25 feet long.

A single mass point representing the payload, which weighs roughly 5,000 pounds, is located at the foot beneath the riser. The ringsail's canopy is composed of various elements.

Radial lines, suspended lines, risers, a vent band, a skirt band, and leading- as well as trailing-edge films are all included in this model of a ringsail parachute.

Smoothing

The structure mesh is very refined and models each individual ring, sail and gore of the parachute.

To accurately identify the locations of stress concentration, a mesh like this is required.The fluid mechanics mesh at the interface is coarser.

We use the FSI-GST described in [61] to generate and update the fluid mechanics mesh at the interface.

Because the size of the parachute vent is so tiny, maintaining one element for gore in that area would have required excessive mesh improvement which should have been beyond the means of flow calculations.

As a result, we choose every other mountain node to represent the rings and each plateau point for the sails in a concentric manner. We select every other valley node for the first ring in order to maintain the element aspect ratios within a suitable range in the direction of longitude.

Figures 2 and 3 depict the structure of the and fluid meshes at the interface for four gores.

Furthermore, we observe that as we approach the parachute's skirt, the surfaces begin to curve to match the paper; as a result, the aspect ratios for the meshes close to the skirt are actually better than what Figures 2 and 3 show. Figures 4 depict the architecture and fluid contacts complete for this initial band.

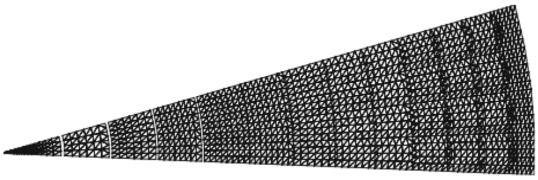	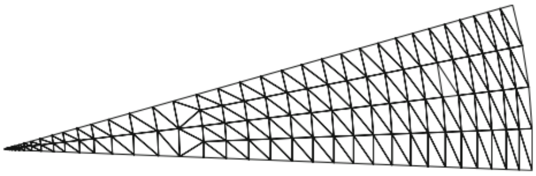
Figure 1. Four-gore structure mesh at the interface	**Figure 2.** Four-gore fluid mesh at the interface.
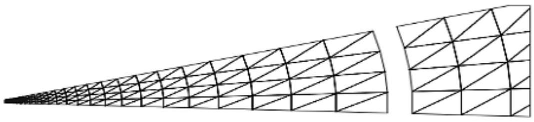	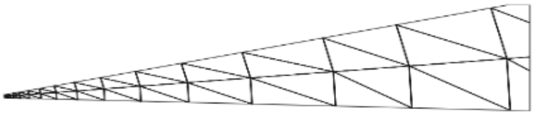
Figure 3. Structure mesh for the first ring.	**Figure 4.** Fluid mesh for the first ring.

Homogenization

We use two homogenized models for geometric porosity.

In the first model, in the fluid mechanics computations, the geometric porosity is represented by a single, uniform porosity for the entire canopy.

A porosity coefficient of 262.6 CFM gives us the expected nominal drag.

A good portion of the results reported in the paper were obtained with this uniform porosity.

We note that these results meet out expectations, and therefore we believe that the model has acceptable accuracy and is attractive because of its simplicity.

We use a locally-varying fabric porosity in the third model to describe its geometric opacity. We divide the canopy into 12 concentric patches and calculate an equivalent fabric- porosity coefficient for each in Figure 5.

Each of the patching has a slit with a portion of a sail or ring on either side.

The first ring is fully included in Patch 1, and the last sail is fully included in Patch 12.
Patch 4 containing four-gore slices depicting the fluid and structural interfaces is seen in Figure 6.

Every patch has a porosity coefficient, which is computed for it. The average of the two porosity coefficients is applied at the border separating the two patches.

We perform a one-time flow calculations at a low Reynolds number, holding the canopy solid, and utilizing a four-gore canopy slice comprising all the sounds and sails, and slits to determine the porosity coefficient for each piece. The problem size is kept manageable by using only a four-gore slice and appropriate restrictions (symmetric conditions in this case) at the boundary of the fluid volume corresponding to the slice.

The structure mesh provides the fluid surface mesh for the four-gore slice, which consists of 2,408 three-node triangle members and 1,464 nodes. The fluid volume mesh for the four-gore slice has 85,101 nodes and 476,410 four-node tetrahedral elements.

The free-stream velocity is 25 feet per second, and the four-gore fluid surface is maintained rigid.

The flow computation is carried out until a fully-developed flow is reached.

Figure 7 shows the flow field, including the flow passing through the slits.

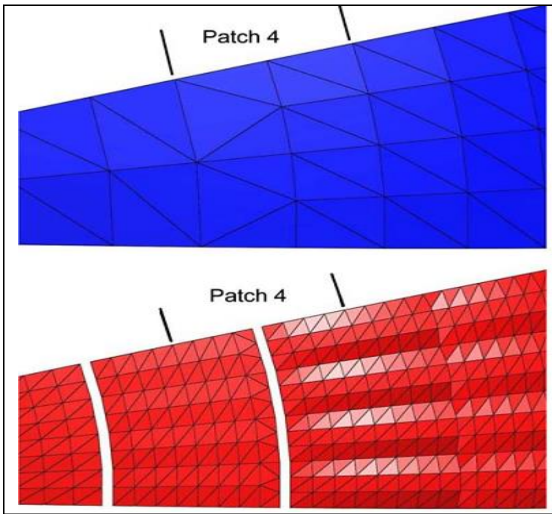

Figure 5. Patch 4 of the four-gore slices of the fluid (top) and structure(bottom) interfaces.

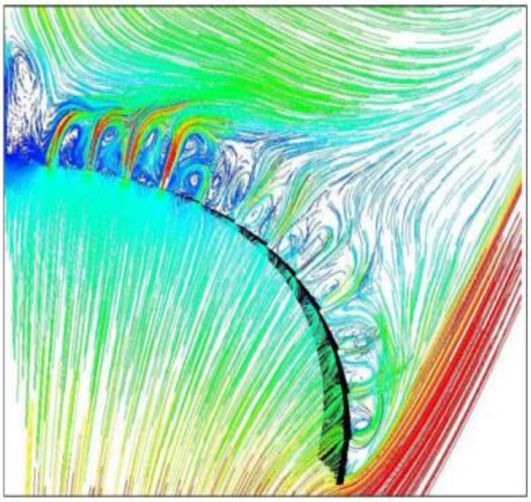

Figure 6. Flow field for the four-gore canopy slice with slits.

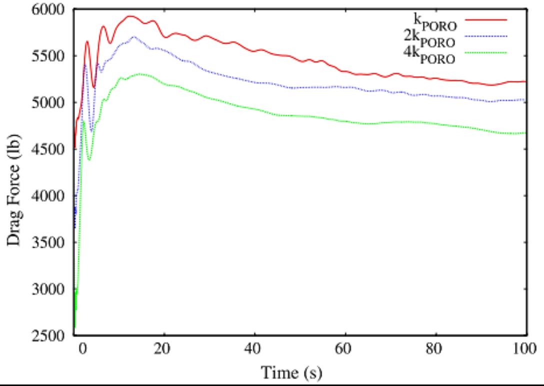

Figure 7. Drag force for the homogenized, smoothened parachute.

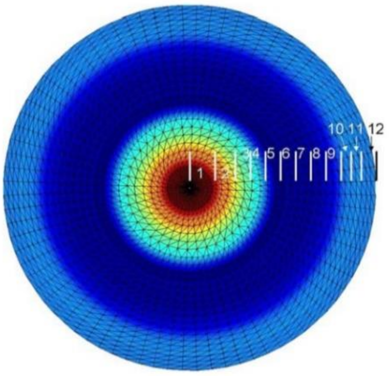

Figure 8. Smoothened, homogenized fluid interface colored by the porosity coefficient.

Next, the porosity parameter for a patch J can be determined using the subsequent formula:

$$\frac{\dot{V}_J}{(A_1)_J} = -(k_{PORO})_J \frac{\Delta F_J}{(A_2)_J} \qquad (1)$$

In this case, the volumetric flow rate across patch J is represented by VJ.

Because of the fabric's porosity, and it includes both the flow through the slits and the flow through the cloth itself.

The area of patch J determined by the smoothened fluid interface is represented by (A1)J, whereas the area determined by the structure interface is represented by (A2)J.

To get the force difference represented by FJ, the temperature discrepancy seen when traversing the patch J is integrated over its area. We find it necessary to calibrate this porosity coefficient by scaling it up or down (using the same calibration factor for all the patches) so that the parachute with the homogenized geometric porosity generates the expected nominal drag of approximately 5,000 lbs.

Figure 8 shows the drag generated by the smoothened and homogenized parachute model with different calibration factors.

We note that scaling up the porosity coefficient by a factor of 2 yields the expected drag.

We therefore use this calibration factor in computations with locally-varying fabric porosity.

Computational Parameters

Leveraging Desktop clusters, the calculations presented here were completed in a fast computational platform. The meshes are generated on a single node of the cluster used.

All computations were completed without any remeshing.

The quasi-direct coupling technique was utilized in each case for solving the fully-discretized, coupled fluid and mechanics of structure equations as well as the mesh-moving coefficients (see to Sect. 5.2 in [47]).

A diagonal preconditioner was applied in conjunction with the GMRES search algorithm [62] to solve the linear equation systems involved at each nonlinear iteration.

To improve the analyses' parallel performance, the meshes are divided.

The METIS [63] algorithm is an underpinning for mesh segmentation.

Using the SUPG test function option WTSA (see Remark 2 in [47]), the mathematical calculations are performed using the SSTFSI-TIP1 approach (see Remarks 5 and 10 in [47]). Equations (9)–(12), (14)–(15), and (17) provide the stabilizing parameters used in [47], with the τSUGN2 term removed from Equation (14).

The properties of air at typical oceanographic conditions are used in all computations.

Section 2 describes the geometry and material characteristics of the structure. The system's mesh is made up of 12,761 two-node cable elements, 28,642 nodes, 48,160 three-node triangle membrane parts, and one payload demonstrate mass.

121,370 nodes and 745,937 four-node hexagonal elements make up the fluid size mesh. With 48,160 elements and 27,120 nodes, the membrane-type portion of this framework creates the interaction with the rest of its components. The homogenized and smoothened fluid interface has 2,320 nodes and 4,520 elements.

The time-step size is 0.0116 s. Six nonlinear repetitions occur during time step, and thirty GMRES repetitions occur per quadratic iterate (Figure 9).

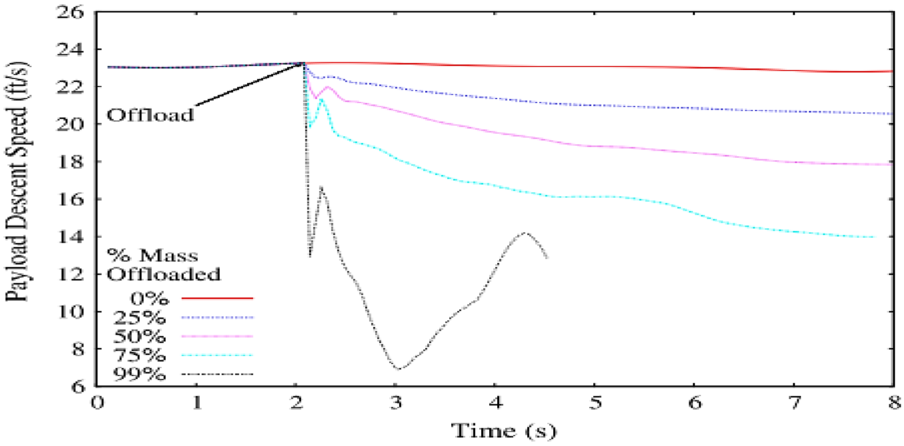

Figure 9. Payload descent speed obtained with the uniform porosity model.

Discharging

It's expected that right before landing, the Orion spacecraft would have to slow down to lose speed. It might not be able to land at its predicted descent speed of 25 feet per second. This would be particularly true if NASA chooses to retrieve the spacecraft on land rather than in the ocean, as they did during the Apollo program. Reducing the truck's weight, also referred to as "offloading," is one method of achieving slower fall speeds during landing. We examine the impact of overloading using current generalized FSI approaches as stated in [47] and more specialized techniques as disclosed in this study. For the homogenized and smoothed fluid interface, uniform and locally-varying porosity modelling are used to simulate the outcomes of overloading. With each of the homogenized porosity models, we study the effect of offloading 25, 50, 75 and 99% of the payload weight.

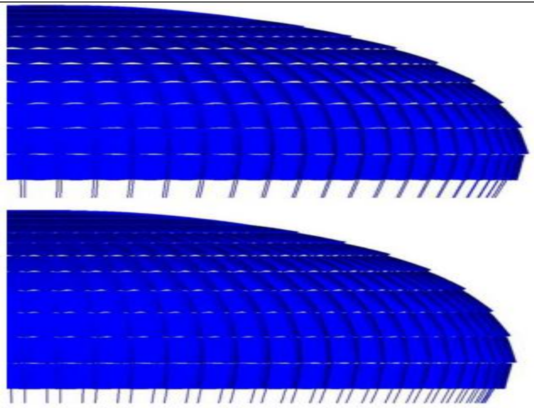

Figure 10. Parachute shape before and about 6 s after the heat shield is dropped

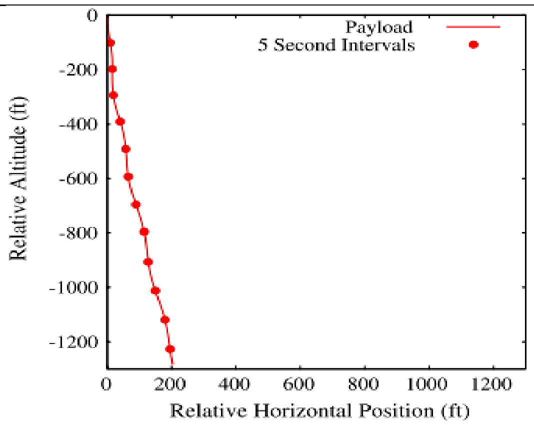

Figure 11. Payload trajectory for the drifting ringsail parachute.

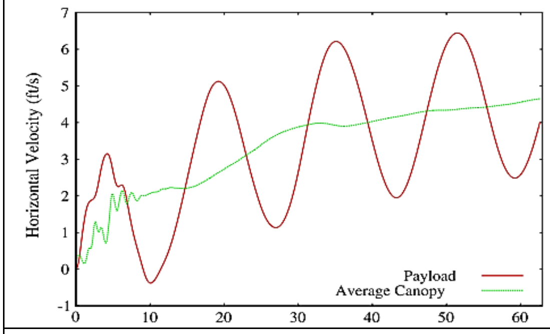

Figure 12. Horizontal velocity for the drifting ringsail parachute.

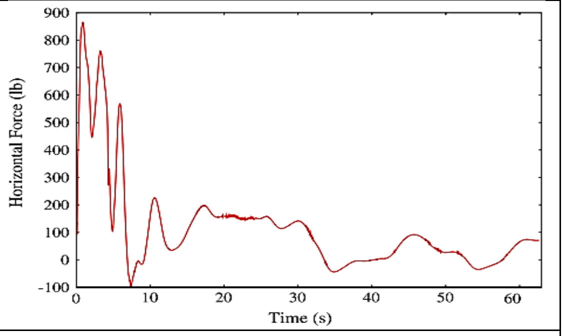

Figure 13. Horizontal force acting on the drifting ringsail parachute.

Figures 10 and 11 show the descent speed and drag obtained with the uniform porosity model. Figures 12 and 13 show the descent speed and drag obtained with the locally-varying porosity model. As expected, the descent speed of the payload decreases with increasing amount of offloaded weight.

We also note that the drag force decreases approximately to the level of the remaining payload weight.

Drifting

Under the assumption that the Orion space vehicle would be recovered on land and not in the ocean, it would be important for the space vehicle to land close to the targeted landing spot.

Excessive drifting of the parachute under the influence of side winds could carry the vehicle away from the targeted landing spot and land it on terrain that is not suitable.

We therefore, using our FSI techniques, study the drifting of the ringsail parachute due to side winds.

In the computation reported in this paper, we assume a side wind of 12.5 ft/s.

We use the uniform porosity model for the homogenized and smoothened fluid interface.

Usually one minute is spent running the mathematical function. Figure 18 shows the payload trajectory.

We note that the payload drifts about 200 ft in a 1,200 ft descent.

Figure 19 shows the horizontal velocity for the payload and the canopy.

We note that the velocities are increasing gradually, and we expect them to, after a sufficiently long duration, reach the side-wind speed of 12.5 ft/s.

Figure 20 shows the horizontal force acting on the canopy.

We observe that it is decreasing gradually, and we expect it to become zero when the parachute horizontal velocity matches the side-wind velocity.

CONCLUSION

We presented our ringsail parachutes FSI simulation.

The design of the paratrooper canopy presents considerable mathematical hurdles due to the geometric complications caused by the "rings" and "sails" utilized in its production.

We went into great detail on the way we handle those numerical difficulties.

The stabilizing space–time FSI (SSTFSI) approach and junction projected strategies, which handle the computation difficulties brought on by the intricate geometric features of the fluid-structure interface is are the foundations of FSI model. The SSTFSI technique is the new-generation space–time FSI method developed recently by the TAFSM to increase the scope and performance of the earlier versions.

The interface projection techniques include the FSI-GST and the HMGP, also developed recently by the TAFSM. The fluid economics mesh is protected from the effects of the geometric complexity of the structure by the FSI-GST and its particular version for parachutes to fall.

By mimicking the geometric porosity of the chute canopy with a locally-varying, "equivalent" fabric porosity, the HMGP allows us to avoid the insoluble complications of that porosity.

During the course of the Orion spacecraft's terminal fall, NASA is anticipated to deploy a trio of ringsail parachutes.

Here, we simulated a single main parachute that would support one-third of the spacecraft's overall weight.

We replicated the process of loading, which involves the removal of the shield of heat in a certain scenario, as well as drifting while being affected by outside headwinds. The aforementioned simulations demonstrate how the mathematical difficulties of the ringsail parachutes' computational issues may be effectively addressed by the SSTFSI technology in conjunction with interface projector technologies.

REFERENCES

1. Tezduyar T, Aliabadi S, Behr M, Johnson A, Mittal S (1993) Parallel finite-element computation of 3D flows. Computer 26:27–36Comput Mech (2008) 43:133–142,141
2. Tezduyar TE, Aliabadi SK, Behr M, Mittal S (1994) Massively parallel finite element simulation of compressible and incompressible flows. Comput Meth Appl Mech Eng 119:157–177
3. Mittal S, Tezduyar TE (1994) Massively parallel finite element computation of incompressible flows involving fluid–body interactions. Comp Meth Appl Mech Eng 112:253–282
4. Mittal S, Tezduyar TE (1995) Parallel finite element simulation of 3D incompressible flows—Fluid–structure interactions. Int J Numer Meth Fluids 21:933–953
5. Johnson AA, Tezduyar TE (1999) Advanced mesh generation and update methods for 3D flow simulations. Computat Mech 23:130–143
6. Kalro V, Tezduyar TE (2000) A parallel 3D computational method for fluid–structure interactions in parachute systems. Comp Meth Appl Mech Eng 190:321–332
7. Stein K, Benney R, Kalro V, Tezduyar TE, Leonard J, Accorsi M(2000) Parachute fluid–structure interactions: 3-D computation. Comp Meth Appl Mech Eng 190:373–386
8. Tezduyar T, Osawa Y (2001) Fluid–structure interactions of a parachute crossing the far wake of an aircraft. Comp Meth Appl Mech Eng 191:717–726
9. Ohayon R (2001) Reduced symmetric models for modal analysis of internal structural-acoustic and hydroelastic-sloshing systems. Comp Meth Appl Mech Eng 190:3009–3019
10. Tezduyar TE, Sathe S, Keedy R, Stein K (2004) Space–time techniques for finite element computation of flows with moving boundaries and interfaces. In: Gallegos S, Herrera I, Botello S, Zarate F, Ayala G (eds) Proceedings of the III international congress on numerical methods in engineering and applied science, CD-ROM, Monterrey, Mexico
11. Torii R, Oshima M, Kobayashi T, Takagi K, Tezduyar TE (2004) Influence of wall elasticity on image-based blood flow simulation. Jpn Soc Mech Eng J Ser A 70:1224–1231 (in Japanese)
12. van Brummelen EH, de Borst R (2005) On the nonnormality of subiteration for a fluid–structure interaction problem. SIAM J Sci Comput 27:599–621
13. Michler C, van Brummelen EH, de Borst R (2005) An interface Newton–Krylov solver for fluid–structure interaction. Int J Numer Meth Fluids 47:1189–1195
14. Gerbeau J-F, Vidrascu M, Frey P (2005) Fluid–structure interaction in blood flow on geometries based on medical images. Comp Struc 83:155–165
15. Tezduyar TE, Sathe S, Keedy R, Stein K (2006) Space–time finite element techniques for computation of fluid–structure interactions.Comp Meth Appl Mech Eng 195:2002–2027
16. Tezduyar TE, Sathe S, Stein K (2006) Solution techniques for the fully-discretized equations in computation of fluid–structure interactions with the space–time formulations. Comp Meth Appl Mech Eng 195:5743–5753
17. Torii R, Oshima M, Kobayashi T, Takagi K, Tezduyar TE (2006) Computer modeling of cardiovascular fluid–structure interactions with the Deforming-Spatial-Domain/Stabilized Space–Time formulation. Comp Meth Appl Mech Eng 195:1885–1895
18. Tezduyar TE, Sathe S, Stein K, Aureli L (2006) Modeling of fluid–structure interactions with the space–time techniques. In: Bungartz H-J, Schafer M (eds) Fluid–structure interaction, vol 53. Lecture notes in computational science and engineering. Springer, Heidelberg, pp 50–81

19. Torii R, Oshima M, Kobayashi T, Takagi K, Tezduyar TE (2006) Fluid–structure interaction modeling of aneurysmal conditions with high and normal blood pressures. Comput Mech 38:482–490
20. Dettmer W, Peric D (2006) A computational framework for fluid–structure interaction: finite element formulation and applications. Comp Meth Appl Mech Eng 195:5754–5779
21. Bazilevs Y, Calo VM, Zhang Y, Hughes TJR (2006) Isogeometric fluid–structure interaction analysis with applications to arterial blood flow. Comput Mech 38:310–322
22. Khurram RA, Masud A (2006) A multiscale/stabilized formulation of the incompressible Navier–Stokes equations for moving boundary flows and fluid–structure interaction. Comput Mech 38: 403–416
23. Kuttler U, Forster C, Wall WA (2006) A solution for the incompressibility dilemma in partitioned fluid–structure interaction with pure Dirichlet fluid domains. Comput Mech 38:417–429
24. Lohner R, Cebral JR, Yang C, Baum JD, Mestreau EL, Soto O(2006) Extending the range of applicability of the loose coupling approach for FSI simulations. In: Bungartz H-J, Schafer M (eds)Fluid–structure interaction, vol 53. Lecture notes in computational science and engineering. Springer, Heidelberg, pp 82–100
25. Bletzinger K-U, Wuchner R, Kupzok A (2006) Algorithmic treatment of shells and free form-membranes in FSI. In: Bungartz H-J, Schafer M (eds) Fluid–structure interaction, vol 53. Lecture notes in computational science and engineering, Springer, Heidelberg,pp 336–355
26. Torii R, Oshima M, Kobayashi T, Takagi K, Tezduyar TE(2007) Influence of wall elasticity in patient-specific hemodynamic simulations. Comp Fluids 36:160–168
27. Masud A, Bhanabhagvanwala M, Khurram RA (2007) An adaptive mesh rezoning scheme for moving boundary flows and fluid–structure interaction. Comp Fluids 36:77–91
28. Sawada T, Hisada T (2007) Fuid–structure interaction analysis of the two dimensional flag-in-wind problem by an interface tracking ALE finite element method. Comp Fluids 36:136–146
29. Wall WA, Genkinger S, Ramm E (2007) A strong coupling partitioned approach for fluid–structure interaction with free surfaces. Comp Fluids 36:169–183
30. Bazilevs Y, Calo VM, Hughes TJR, Zhang Y (2008) A fully-integrated approach to fluid–structure interaction. Comput Mech (in preparation)
31. Stein KR, Benney RJ, Kalro V, Johnson AA, Tezduyar TE (1997) Parallel computation of parachute fluid–structure interactions. In: Proceedings of AIAA 14th aerodynamic decelerator systems technology conference, AIAA paper 97-1505, San Francisco
32. Tezduyar TE (1992) Stabilized finite element formulations for incompressible flow computations. Adv Appl Mech 28:1–44
33. Tezduyar TE, Behr M, Liou J (1992) A new strategy for finite element computations involving moving boundaries and interfaces—the deforming-spatial-domain/space–time procedure: I. The concept and the preliminary numerical tests. Comp Meth Appl Mech Eng 94:339–351
34. Tezduyar TE, Behr M, Mittal S, Liou J (1992) A new strategy for finite element computations involving moving boundaries and interfaces—the deforming-spatial-domain/space–time procedure: II. Computation of free-surface flows, two-liquid flows, and flows with drifting cylinders. Comp Meth Appl Mech Eng 94:353–371
35. Tezduyar TE (2003) Computation of moving boundaries and interfaces and stabilization parameters. Int J Numer Meth Fluids 43:555–575
36. Hughes TJR, Brooks AN (1979) A multi-dimensional upwind scheme with no crosswind diffusion. In: Hughes TJR (ed) Finite element methods for convection dominated flows, AMD-vol 34.ASME, New York, pp 19–35
37. Brooks AN, Hughes TJR (1982) Streamline upwind/Petrov-Galerkin formulations for convection dominated flows with particular emphasis on the incompressible Navier–Stokes equations. Comp Meth Appl Mech Eng 32:199–259
38. Tezduyar TE, Mittal S, Ray SE, Shih R (1992) Incompressible flow computations with stabilized bilinear and linear equal-order-interpolation velocity-pressure elements. Comp Meth Appl MechEng 95:221–242 123 142 Comput Mech (2008) 43:133–142

39. Hughes TJR, Franca LP, Balestra M (1986) A new finite element formulation for computational fluid dynamics: V. Circumventing the Babuška–Brezzi condition: a stable Petrov–Galerkin formulation of the Stokes problem accommodating equal-order interpolations. Comput Meth Appl Mech Eng 59:85–99
40. Tezduyar TE, Behr M, Mittal S, Johnson AA (1992) Computation of unsteady incompressible flows with the finite element methods space–time formulations, iterative strategies and massively parallel implementations. In: New methods in transient analysis, PVP-vol246/AMD-vol 143, ASME, New York, pp l7–24
41. Johnson AA, Tezduyar TE (1994) Mesh update strategies in parallel finite element computations of flow problems with moving boundaries and interfaces. Comput Meth Appl Mech Eng 119:73–94
42. Johnson AA, Tezduyar TE (1997) Parallel computation of incompressible flows with complex geometries. Int J Numer Meth Fluids24:1321–1340
43. Tezduyar T (2001) Finite element interface-tracking and interface capturing techniques for flows with moving boundaries and interfaces. In: Proceedings of the ASME symposium on fluid-physics and heat transfer for macro- and micro-scale gas–liquid and phase-change flows (CD-ROM), ASME paper IMECE2001/HTD-24206,ASME, New York
44. Tezduyar TE (2003) Stabilized finite element formulations and interface-tracking and interface-capturing techniques for incompressible flows. In: Hafez MM (ed) Numerical simulations of incompressible flows. World Scientific, New Jersey, pp 221–239
45. Stein K, Tezduyar T, Benney R (2003) Mesh moving techniques for fluid–structure interactions with large displacements. J Appl Mech 70:58–63
46. Tezduyar TE, Sathe S, Senga M, Aureli L, Stein K, Griffin B (2005) Finite element modeling of fluid–structure interactions with space–time and advanced mesh update techniques. In: Proceedings of the 10th international conference on numerical methods in continuum mechanics (CD-ROM), Zilina, Slovakia
47. Tezduyar TE, Sathe S (2007) Modeling of fluid–structure interactions with the space–time finite elements: solution techniques. Int J Numer Meth Fluids 54:855–900
48. Mittal S, Tezduyar TE (1992) A finite element study of incompressible flows past oscillating cylinders and aerofoils. Int J Numer Meth Fluids 15:1073–1118
49. Stein K, Benney R, Tezduyar T, Kalro V, Leonard J, Accorsi M (1999) 3-D computation of parachute fluid–structure interactions: performance and control. In: Proceedings of CEAS/AIAA 15th aerodynamic decelerator systems technology conference, AIAA paper 99-1714, Toulouse, France
50. Stein K, Benney R, Tezduyar T, Kalro V, Potvin J, Bretl T (1999) Fluid–structure interaction simulation of a cross parachute: comparison of numerical predictions with wind tunnel data. In: Proceedings of CEAS/AIAA 15th aerodynamic decelerator systems technology conference, AIAA Paper 99-1725, Toulouse, France
51. Stein K, Benney R, Tezduyar T, Potvin J (2001) Fluid–structure interactions of a cross parachute: numerical simulation. Comp Meth Appl Mech Eng 191:673–687
52. Stein KR, Benney RJ, Tezduyar TE, Leonard JW, Accorsi ML (2001) Fluid–structure interactions of a round parachute: modeling and simulation techniques. J Aircraft 38:800–808
53. Tezduyar TE (2003) Stabilized finite element methods for flows with moving boundaries and interfaces. HERMIS Int J Comp Math Appl 4:63–88
54. Tezduyar TE (2004) Finite element methods for fluid dynamics with moving boundaries and interfaces. In: Stein E, De Borst R, Hughes TJR (eds) Encyclopedia of computational mechanics, vol 3. Fluids, Chap 17. Wiley, New York
55. Tezduyar TE (2004) Moving boundaries and interfaces. In: Franca LP, Tezduyar TE, Masud A (eds) Finite element methods: 1970's and beyond, CIMNE, Barcelona, pp 205–220
56. Tezduyar TE (2007) Finite elements in fluids: special methods and enhanced solution techniques. Comp Fluids 36:207–223
57. Tezduyar TE, Sathe S, Cragin T, Nanna B, Conklin BS, Pausewang J, Schwaab M (2007) Modeling of fluid–structure interactions with the space–time finite elements: arterial fluid mechanics. Int J Numer Meth Fluids 54:901–922

58. Tezduyar TE, Pausewang J, Sathe S (2007) FSI modeling of sails. In: Onate E, Garcia J, Bergan P, Kvamsdal T (eds) Marine 2007, CIMNE, Barcelona
59. Tezduyar TE, Sathe S, Schwaab M, Conklin BS (2007) Arterial fluid mechanics modeling with the stabilized space–time fluid–structure interaction technique. Int J Numer Meth Fluids. DOI:10.1002/fld.1633
60. Tezduyar TE, Sathe S, Pausewang J, Schwaab M, Crabtree J, Christopher J (2007) Air–fabric interaction modeling with the stabilized space–time FSI technique. In: Proceedings of the third Asian-Pacific congress on computational mechanics (CD-ROM), Kyoto
61. Tezduyar TE, Sathe S, Pausewang J, Schwaab M, Christopher J, Crabtree J (2008) Interface projection techniques for fluid–structure interaction modeling with moving-mesh methods. Comput Mech. doi:10.1007/s00466-008-0261-7
62. Saad Y, Schultz M (1986) GMRES: a generalized minimal residual algorithm for solving nonsymmetric linear systems. SIAM J Sci Stat Comput 7:856–869
63. Karypis G, Kumar V (1998) A fast and high quality multilevel scheme for partitioning irregular graphs. SIAM J Sci Comput 20:359–392